A Benchtop Simulator for Evaluating Astronomical Observations with Object Generation and Point Spread Function Engineering

Megan Birch
Georgia State University and Georgia Tech Research Institute
Leticia García Varela
Georgia State University and Instituto de Astrofísica de Canarias

Fabien Baron
Georgia State University

ABSTRACT

The Advanced Reconnaissance of Earth-orbiting Satellites (ARES) system is a versatile optical benchtop designed to simulate a range of environmental and optical conditions to study the effects of various atmospheric disturbances and wavefront sensing techniques. This paper presents advancements to the ARES system by integrating an object generation module through phase modulation techniques and a Point Spread Function (PSF) "dark hole" engineered tool using the Hybrid Optical Telescope (HOT). In the extended setup, the object generator utilizes principles of Fourier optics to manipulate wavefronts with the goal of generating the behavior of space targets through the atmosphere, such as satellites, debris, and low-intensity objects, enhancing our capability to simulate optical phenomena. The HOT system leverages "dark hole" engineering for low-intensity object detections and adaptive optics (AO) for turbulence correction capabilities. The system also explores polarization rotation and complex phase modulation for improved amplitude control to form high-fidelity simulations of space objects. This scalable optical benchtop offers significant applications in space surveillance, satellite imaging, and scientific research, contributing to improved Space Domain Awareness (SDA) and the protection of space assets.

1. INTRODUCTION

The Advanced Reconnaissance of Earth-orbiting Satellites (ARES) system is a versatile benchtop testbed designed to simulate atmospheric turbulence and validate techniques for high-resolution ground-based imaging of near-Earth orbiting satellites [1]. ARES is equipped with a wide range of optical components, including deformable mirrors (DMs), Shack-Hartmann wavefront sensors, and spatial light modulators (SLMs), which together allow it to simulate and correct for the effects of atmospheric distortion. This paper focuses on two advancements made to the ARES benchtop design including a Point Spread Function (PSF) engineering tool and an object generation module.

To increase the resolution and visibility of both celestial and Earth-orbiting objects, the astronomical community has traditionally moved towards constructing larger aperture telescopes, such as the Keck, Gran Telescopio de Canarias, and the Extremely Large Telescope [2]. While larger diameters facilitate greater photon capture and improved angular resolution, they introduce formidable challenges regarding overall construction and optimal performance. Addressing these challenges, modern telescopes have adopted segmented mirrors combined with adaptive optics (AO) to create lighter, cost-efficient systems capable of high-precision wavefront distortion corrections [3], further revolutionizing this field, allowing for more precise wavefront corrections and improved imaging capabilities [4]. This innovation underpins the development of the Hybrid Optical Telescope (HOT), a Fizeau imaging distributed aperture telescope, which leverages segmented mirrors and AO to not only provide capabilities for mitigating atmospheric turbulence, but also to enhance resolution by using lightweight mirrors and a tensegrity support structure [5]. Furthermore, the HOT's ability to engineer a dark hole in the Point Spread Function (PSF) enables the ability for detecting faint sources adjacent to bright objects.

In high-contrast imaging applications, such as exoplanet detection or Space Domain Awareness (SDA), observing faint sources near bright objects presents a significant challenge due to the overwhelming brightness of the primary source and the ability to engineer a dark hole in the PSF through the HOT system offers a powerful solution [6]. By

dynamically correcting wavefront distortions and manipulating the PSF, HOT systems can suppress light from a bright object in targeted regions of the image, creating an area where the light is minimized [7]. This dark hole improves contrast and allows for the detection of faint sources adjacent to the bright object, enhancing the system's capability for resolving fine details in challenging observational environments [8]. This technique has broad applications in fields such as astronomy and space surveillance, where the ability to isolate and detect faint objects is crucial [9].

Building upon the HOT framework, this paper introduces an object generation module designed to simulate a diverse array of celestial and man-made objects as virtual inputs to the ARES setup under various atmospheric and observational scenarios. Although the HOT system and the object generation module share the same optical components and SLMs, they function as two distinct systems within the benchtop environment. The object generation module uses Fourier optics principles [10] combined with an optimization phase model to simulate the phases required for generating holograms of desired objects [11]. Both systems are employed within the ARES benchtop, utilizing three SLMs. These two distinct systems form the foundation of a compact, controlled setup for modeling and correcting atmospheric turbulence and studying its effects on propagating wavefronts [12, 13]. The ability to simulate space objects, such as satellites and debris, with high fidelity on a benchtop enables the validation of algorithms and enhances our ability to monitor and mitigate orbit-based threats and potential collisions.

2. HOT APERTURE

The ARES optical circuit enables the exploration of a broad range of conditions affecting the light path, providing a platform for studying the effects of atmospheric disturbances and wavefront sensing techniques to correct such aberrations [1]. In this research, we utilized the ARES benchtop to modify the PSF of the HOT system. By correcting for optical aberrations and reshaping the PSF, we created a hole close to the center of the image.

The goal was to create a dark region in the main PSF that, with sufficient contrast, would reveal the peak of a fainter object otherwise obscured by the intensity of a brighter source. This dark hole was achieved by applying a limited set of Zernike polynomials to reshape the PSF, significantly enhancing contrast in the targeted region compared to the original diffraction-limited PSF. Initially, 3 Zernike modes were selected to replicate the degrees of freedom of non-deformable mirrors (piston, tip, and tilt) in the HOT aperture. However, this was later expanded to 40 modes as a theoretical exploration to improve efficacy. Although in practise this cannot be performed by regular non-deformable mirrors in a telescope, it can be tested in the benchtop using a SLM. Our first intention was to achieve an intensity

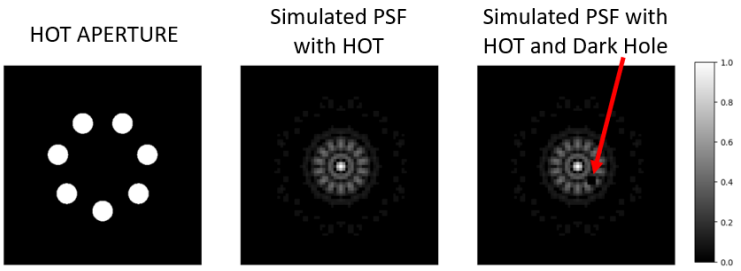

Fig. 1: Left: The HOT aperture used in the lab with seven sub-apertures. Middle: The theoretical PSF generated in our simulation, based on the aperture geometry. Right: The simulated PSF featuring a dark hole, which serves as the target for replication in the benchtop setup. The dark hole is engineered to enhance the visibility of low-intensity objects by suppressing light from surrounding brighter sources. The figure illustrates the desired PSF structure, which will be achieved through precise phase modulation and adaptive optics techniques. Both PSF images are the square root of the original simulated values, divided by the maximum, creating comparable intensity values ranging from 0 and 1.

distribution shown on the right in Figure 1, however it was observed in order to keep the exact structure of the PSF, we would need a larger amount of Zernike modes or sub-apertures, as shown in Figure 2, where we can see how employing 40 Zernikes produces a PSF more similar to the expected middle image from Figure 1.

The location of the dark region in our experiment was selected on one of the 'petals' or aperture holes, as these high-intensity areas are where dim objects are most likely to be obscured by brighter sources. We chose a dark hole with a diameter of 3 pixels for two reasons: smaller holes are easier to achieve as they minimally disturb the PSF, and

the size is sufficient to distinguish the potential peak of a weaker object. These simulated results demonstrate the effectiveness of using Zernike polynomials for PSF shaping, allowing us to create a dark hole near the PSF core. The model indicated strong potential in fields where dim objects are frequently overshadowed by brighter ones, such as satellites or binary star systems, making it highly relevant for both astronomical and defense applications.

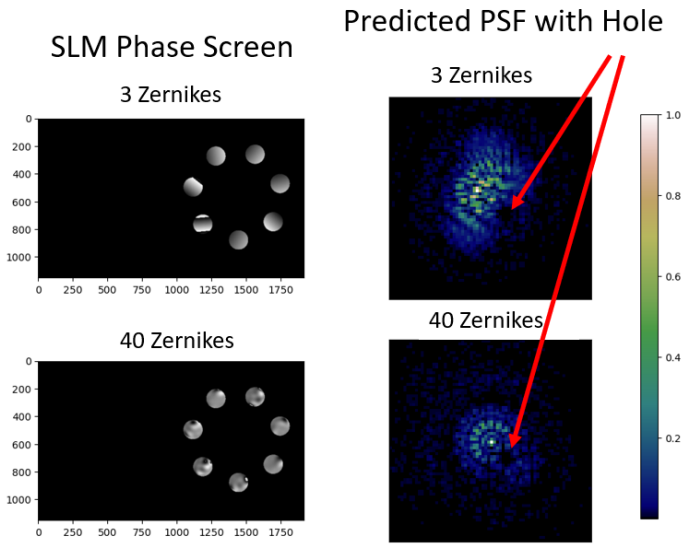

Fig. 2: Left column shows the phase screens optimized to reproduce the ideal PSF with the hole from Figure 1. Right column identifies their corresponding PSFs predicted by the model. Top row uses a combination of 3 Zernike modes while the bottom row uses 40. The colorbar shows the range of intensity values of the PSFs, divided by their maximum intensity value to display comparable values between 0 and 1, while the phase screens are scaled and wrapped between $[-\pi, \pi]$ and mapped to an 8-bit scheme between 0 and 255 as required when implementing onto the SLMs. For the HOT experiment, only the first pass on SLM 3 is used, as we are focusing solely on one phase modifications. This explains why the left half of the screen remains empty. Pixel numbers are displayed on the x and y axes to show the location of the beam on the SLM phase screen.

2.1 Phase Modifications

In the benchtop experiment, we replicate the conditions of a space-based telescope, where light reaches the aperture without distortion from atmospheric effects. Using the ARES system to manipulate the optical field phase, we employed three SLMs. SLM 1 and 2 corrected optical aberrations prior to the HOT aperture, while SLM 3 provided additional phase correction and PSF shaping after the wavefront passed through the telescope pupil.

Phase Diversity (PD) was employed for modeling the wavefront aberrations of the beam, resulting in a static surface of non-constant phase values [1]. With those quantities, we created correcting phase screens using the negative values of the model's surface to flatten the reflected beam off of the SLMs.

To determine the optimal phase for producing a PSF with a hole, a model was developed to identify the combination of Zernike polynomials for the phase at the telescope aperture whose PSF minimized a defined loss function ($\mathscr{L}$), including the two terms: *contrast* and *fidelity* [14]. The contrast term ($\tilde{C}$) measured the intensity rate between the core and the hole, while the fidelity term (F) quantified the difference between the simulated PSF and the desired PSF outside the core and the hole. The loss function is described by the following equation:

$$\mathscr{L} = \tilde{C} + F = \frac{I_H}{I_C} + \sum_x \sum_y \|I_m(x,y) - I_i(x,y)\|^2 \tag{1}$$

where I_H is the intensity in the hole, I_C is the intensity in the core, x and y are the coordinates of each pixel outside the core and the hole, I_m is the intensity of the simulated PSF, and I_i is the intensity of the desired PSF. This work implements an advanced optical simulation in the Julia software language to simulate the PSF modification required for the HOT system. The diameters and centers of each HOT sub-aperture are initially mapped onto SLM 3. This

information is then processed by the model to generate a mask with identical proportions, ensuring Nyquist sampling conditions are met. Here, we assume unit amplitude across the pupil.

The model further applies complex phase modulations using a specified number of Zernike modes to build PSFs with a hole in a determined location. The optimization process then iteratively adjusts each Zernike coefficient to minimize $\mathscr{L}$, particularly focusing on the suppression of light within a designated location, while also trying to maintain the original HOT PSF structure. The optimization utilizes the `OptimPackNextGen` Julia package for automatic differentiation and gradient-based optimization. We ran two simulations, one using only piston, tip and tilt, and a second one with the first 40 Zernike modes, indexed according to the Noll numbering scheme.

Finally, data generated during the simulations, including the predicted contrast between the core and hole as well as the final values of $\tilde{C}$ and F, are saved for further analysis and visualization. The optimized phase is exported as a bitmap image, to apply on the SLM for experimental validation on the benchtop. The left images in Figure 2 are examples of these phase screens, applied onto SLM 3, followed by the modeled PSF images on the right, illustrating the expected observations on the optics bench. The optimized phase (left plots in Figure 2) were combined on the third SLM with its own PD corrections to achieve an observed PSF with hole closer to the predicted simulations, displayed in the right of Figure 2. SLMs 1 and 2 had their own PD corrections applied exclusively to flatten the beam and were not combined with any other phase screens for this experiment.

3. OBJECT GENERATOR

The object generator design refers to an optical system or module that uses wavefront manipulation techniques, such as phase modulation, to create virtual objects or simulate specific optical targets on an experimental bench setup. This tool allows for the controlled generation of wavefronts that replicate the appearance and behavior of spaceborne objects, such as satellites, debris, and faint celestial bodies, as they might appear through atmospheric disturbances. An object generator implemented into the ARES system contains capabilities for simulating a wide range of objects to study atmospheric effects and improve observation techniques in astronomy and SDA.

As an addition to the ARES benchtop setup, a one-phase or one pass object generator was initially implemented, utilizing only one-phase modulation generated from the specified image and applying this phase onto the SLM requiring only one Fourier transform to produce the hologram. This design was further refined by introducing modifications to the third SLM, where a second phase is applied as the system reflects back onto the same SLM (referred to as SLM 3.5). This enhancement enables the generation of arbitrary complex wavefronts using a high-fidelity dual-phase modulation technique for precise hologram generation [11]. The dual-phase technique allows for precise control over phase and amplitude, essential for simulating complex optical scenarios and enhancing astronomical observations in the ARES system. By employing this method on a benchtop setup, this research aimed to advance the capabilities of wavefront propagation tools in the lab as well as simulate space objects for future applications such as imaging two closely spaced objects of significantly different luminosities.

Although deploying single phase modulation tools, such as diffractive optical elements, exist for encoding optical fields, they often require trade-offs such as increased speckle noise, lowered efficiency, the generation of unwanted diffraction orders, and a loss of independent control over amplitude and phase. In comparison, a dual-phase modulation technique, breaks up the amplitude and phase encoding of a complex field to enable holographic reconstructions with higher fidelity and reduced noise [11]. This system incorporates additional aperture masks to remove unwanted high spatial frequencies, as well as a half-wave plate for polarization control of the incoming and reflected beams from the SLMs [15]. These modifications provide insight into improving the quality of the object generation process to optimize the system integrated into the ARES benchtop.

3.1 Theoretical Background

Wavefront manipulation tools provide precise control over optical field characteristics. Among the available methods, a dual-phase, dual-pass modulation system utilizing SLMs [16] was selected for its ability to independently modulate both spatial amplitude and phase distributions, as well as its potential for 3D volume hologram construction. This dual-phase system converts spatial light distributions into frequency components [17], facilitating the simulation and reconstruction of complex objects.

The dual-phase method offers improvements over the one-phase method in controlling both amplitude and phase independently, resulting in improved image quality and reduced noise [11]. In the one-phase method, encoding both

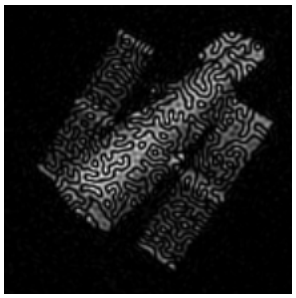

Fig. 3: Simulated image of HST using the one-phase optimization model.

Fig. 4: Simulated image of HST using the dual-phase optimization model.

amplitude and phase on a single SLM often introduces compromises, such as increased speckle noise and reduced fidelity of high spatial frequencies [1]. Figures 3 and 4 show the difference in the optimization model's generating the Hubble Space Telescope (HST) with one phase versus two phases. The dual-phase optimizing technique produces a more resolved target with finer details. Note here the orientation of the dual-phase image is flipped due to the extra Fourier transform and SLM reflection that occurs compared to the one-phase or one-pass generated image.

This method of wavefront generation must also account for the limitations imposed by band-limited systems, a challenge similarly addressed in blind deconvolution techniques [18]. By contrast, the dual-phase approach separates the modulation tasks between two phase elements placed in conjugate Fourier planes. The first phase mask shapes the amplitude, while the second corrects the phase, allowing for more precise control of the wavefront.

3.2 Mathematical Framework: Complex Wave Fields and Fourier Optics

An optical field in the object plane can be expressed as the wave field [11]:

$$a(x,y) = |a(x,y)|e^{j\Theta(x,y)} \tag{2}$$

where $a(x,y)$ represents the optical field in the object or spatial domain, $|a(x,y)|$ signifies the absolute amplitude in the spatial domain, and $\Theta(x,y)$ denotes the phase for that optical field in the object plane. Here, x and y are spatial coordinates, and j is the imaginary unit. The transformation of the optical field in the spatial domain to the frequency domain is carried out via a Fourier transform. The complex optical field in the frequency domain or Fourier plane is expressed as:

$$A(u,v) = \mathscr{F}\{a(x,y)\} = \mathscr{F}\{|a(x,y)|e^{-j\Theta(x,y)}\} = |a(x,y)| \int_{-\infty}^{\infty}\int_{-\infty}^{\infty} e^{-j2\pi(ux+vy)}dxdy \tag{3}$$

where $A(u,v)$ is the optical field in the frequency domain, and u and v are the frequency variables corresponding to x and y. The corresponding Fourier transform pair is then:

$$a(x,y) = \mathscr{F}^{-1}\{A(u,v)\} = \mathscr{F}^{-1}\{|A(u,v)|e^{j\theta(u,v)}\} = |A(u,v)| \int_{-\infty}^{\infty}\int_{-\infty}^{\infty} e^{j2\pi(ux+vy)}dudv \tag{4}$$

where F^{-1} represent the inverse Fourier transform and θ indicates the phase of the optical field in the frequency domain.

3.3 Image Reconstruction and Optimization Model Utilizing Two Phases

To modulate the object generated field, we use equation 4 with the annotation $a_O(x,y)$ where $|A_O(u,v)|$ is the object modulus and $\theta_O(u,v)$ is the phase corresponding to the generated object in the frequency domain. Similarly the object generated Fourier transformed field from equation 4 is represented by $A_O(u,v)$ with $|a_O(x,y)|$ as the absolute amplitude in the spatial domain and $\Theta_O(x,y)$ as the phase in the spatial domain. The laser complex optical field will be represented by the same equation and annotation, but instead using $|A_L(u,v)|$ as the laser beam's modulus, $\theta_L(u,v)$

as the laser beam's represented phase in the Fourier domain, $|a_L(x,y)|$ as the laser amplitude in the spatial domain and $\Theta_L(x,y)$ as the laser phase in the spatial domain.

$a_o(x,y)$ can be directly shaped by the element θ_O in the Fourier plane on the SLM phase screen, but not its amplitude. Thus, the modulus of the object field, must be created by Fourier transforming a phase generated from an initial amplitude; in this case, the laser amplitude $|a_L(x,y)|$ by using a phase optimization model. Given this information, we can generate the first phase on the SLM, ψ [19]. When this generated phase is superimposed with the laser amplitude in the pupil plane, $|a_L(x,y)|$, followed by a Fourier transform, the modulus of the generated object in the Fourier domain, plus a randomly distributed phase ϕ caused by this process of generating the first phase will be produced.

We can then generate a second phase placed on the second half of the SLM, β, to superimpose with the generated object modulus, $|A_o(u,v)|$, followed by a Fourier transform to produce the final generated object of interest represented by $(o(x,y))$. This method generates the desired complex field represented as $O(u,v)$ behind the second phase mask, β. Theoretically, $o(x,y)$ should be equal to $a_o(x,y)$, however due to the inherent limitations of Fourier optics and the current model, the resulting wavefront will slightly differ from the simulated one. To distinguish between the two, $o(x,y)$ is used to represent the final hologram produced by the object generator benchtop, and $a_o(x,y)$ will represent the original image in intensity form from which the phases were generated. The second phase, β, is calculated to remove any extraneous phase ϕ from the object generator, caused by the first pass on the SLM, so that only the desired object is produced. Hence, the phase β is calculated by:

$$\beta = \theta_o - \phi \tag{5}$$

The two phases were generated using a phase optimization model in the programming language Julia. The goal of this optimization process is to minimize any residual phase introduced by the first phase on SLM 3 and ensure the final output in the object plane matches the intended output field. The calculated phases from the model along with the simulated modulus is shown in Figure 5. Because SLMs are restricted to discrete pixel levels, the phases must be generated with values from 0 to 2π with 8-bits. This restriction must be applied to the final modeled image for an accurate comparison to the benchtop. The model follows the below process to generate the desired phases.

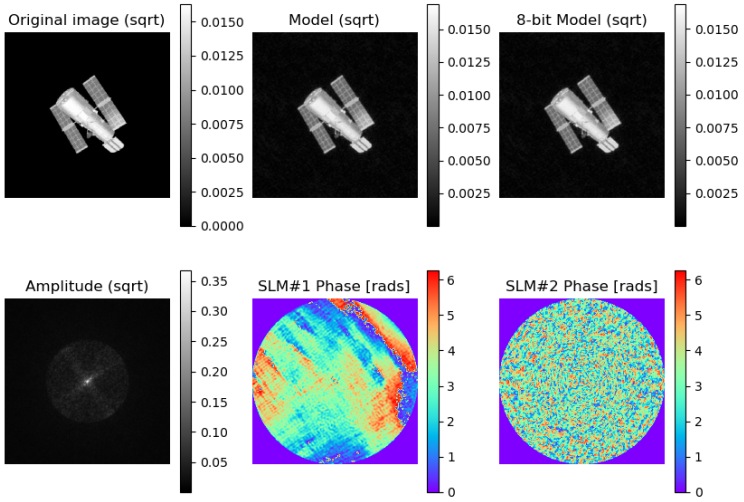

Fig. 5: Generated output from the simulated phase optimization model for an image of HST. The top left shows the original image with an optical field known as $a_o(x,y)$. To the right shows the modeled HST image representing the output for the object generator benchtop as well as the corresponding 8-bit image, due to the SLM restrictions, known as $o(x,y)$. The modulus generated by the Fourier transform of the first phase, ψ, is located on the bottom left. To the right represents phase one, placed on the first half of the SLM sensor, followed by phase two, β, placed on the second half of the third SLM sensor (labeled as SLM 3.5). The grey scales map the intensity values of the pixels in the square-root transformed image to shades of gray located in the top row. The amplitude map and the colorbar in the second row provide a reference for the range of phase values (in radians) or amplitude values. These phases were then saved as bitmaps; scaled and wrapped between $[-\pi,\pi]$ and mapped to an 8-bit scheme between 0 and 255.

The optimization model uses $|a_L(x,y)|$ and $a_o(x,y)$ in the spatial domain to produce a phase that when Fourier transformed, forms the expected $|A_o(u,v)|$ modulus. The resulting field after this phase is transformed to the frequency domain and is represented as:

$$A_o(u,v) = \mathscr{F}\left\{|a_L(x,y)|e^{j\psi(x,y)}\right\} = |A_o(u,v)|e^{j\phi(u,v)} \tag{6}$$

Here, $\phi(u,v)$ is the phase introduced by the first phase screen and $A_o(u,v)$ represents the intermediate optical field in the frequency domain after applying the first phase screen which is also equal to the object field in the spatial domain. Because there are two unknowns, $\psi(u,v)$ and $\phi(u,v)$, an optimization parameter is used to calculate these values in the model. $\beta(u,v)$ is then calculated using equation 6 to correct for the extraneous phase introduced by the first SLM phase screen. After applying the second phase screen, $\beta(u,v)$, to the modulus of the object field $|A_O(u,v)|$ in the frequency domain, the final object field in the spatial domain, $o(x,y)$, is generated by the inverse Fourier transform:

$$o(x,y) = \mathscr{F}^{-1}\left\{|A_O(u,v)|e^{j(\theta_O(u,v)-\phi(u,v))}\right\} = \mathscr{F}^{-1}\left\{|\mathscr{F}\left\{|a_L(x,y)|e^{j\psi(x,y)}\right\}|e^{j(\theta_O(u,v)-\phi(u,v))}\right\} \tag{7}$$

4. EXPERIMENTAL SETUP

The ARES design with the addition of the HOT system and object generator module is illustrated in Figure 6. The HOT system begins at SLM 2 and is combined with the object generator setup beginning at the 4th pupil relay. The HOT system and the one-phase object generator utilizes the one SLM pass off of SLM 3, while the complex object generator setup utilizes the first and second pass off of SLM 3.5.

The ARES system operates on the principle of relaying the initial pupil, a circular aluminum aperture with a diameter of 10 mm, onto the screens of the first two SLMs, maintaining consistent height and size throughout. In this setup, a laser serves as a generic point source, and to simulate the long optical path to the Hybrid Optical Telescope, the light is collimated using a lens before passing through the aluminum aperture, which represents the entrance aperture of a telescope system. The SLMs are then employed to manipulate the complex phase of the wavefront at the HOT by relaying the entrance pupil onto the HOT system. Following SLM 2, a series of lenses relay the initial pupil to the HOT aperture and ultimately to a third SLM, which is used to create a dark hole in the HOT's PSF. The first 4F system, consisting of two lenses separated by the sum of their focal lengths (4F), are used to perform a Fourier transform enabling manipulation of light in both the spatial and frequency domain. Following SLM 2 (the third 4F system overall) magnifies the beam sufficiently to fully illuminate the HOT aperture, which has an external diameter of 36 mm and is located at the image plane of SLM 2. This aperture is only used for the HOT experiment, and is removed for the object generator. A subsequent 4F system reduces the beam diameter and relays the pupil to a new position where a 7 mm aperture is placed, ensuring that the beam, along with its second pass employed in the object generator, fits within the third SLM. The pupil is then relayed once more by the fifth 4F system onto SLM 3.

The HOT system utilizes only the 36mm aperture and does not use the second pass. For the HOT experiments, the 7mm pupil is removed and the beam is relayed onto the SLM followed by a Fourier transform and imaged onto a camera sensor. However, for the object generator we remove the HOT aperture and use a smaller 7mm pupil, to ensure both phases in the dual-phase system fit on the third SLM with a sensor size of 1920x1152 and pixel size of 8 microns.

All SLMs and pupils are positioned at the image planes of their preceding SLMs/pupils, ensuring that the manipulated wavefront retains the same field configuration as it had at the initial 10 mm aluminum aperture. ARES leverages this setup to study the effects of atmospheric turbulence by simulating two independent layers of turbulence—one on each SLM. Additionally, the SLMs are utilized to correct aberrations in the beam, ensuring the wavefront reaching the HOT aperture is as free from distortions as possible. Phase diversity techniques are applied to each SLM to correct these aberrations. The initial HOT benchtop does not utilize SLM 1 and 2 for turbulence simulation.

For phase corrections, phase screens generated through PD are applied to the specific pixels on each SLM where the beam interacts. To accurately identify the illuminated pixels, the beam was pre-mapped, as were the HOT sub-apertures, allowing for precise construction of the phase screen on the pre-determined pixels. For manipulations of the HOT PSF, the optimized phase to create the dark hole is applied exclusively on SLM 3, along with its corresponding corrections, to enhance the PSF structure. Finally, half-wave plates are placed before each SLM to ensure that the

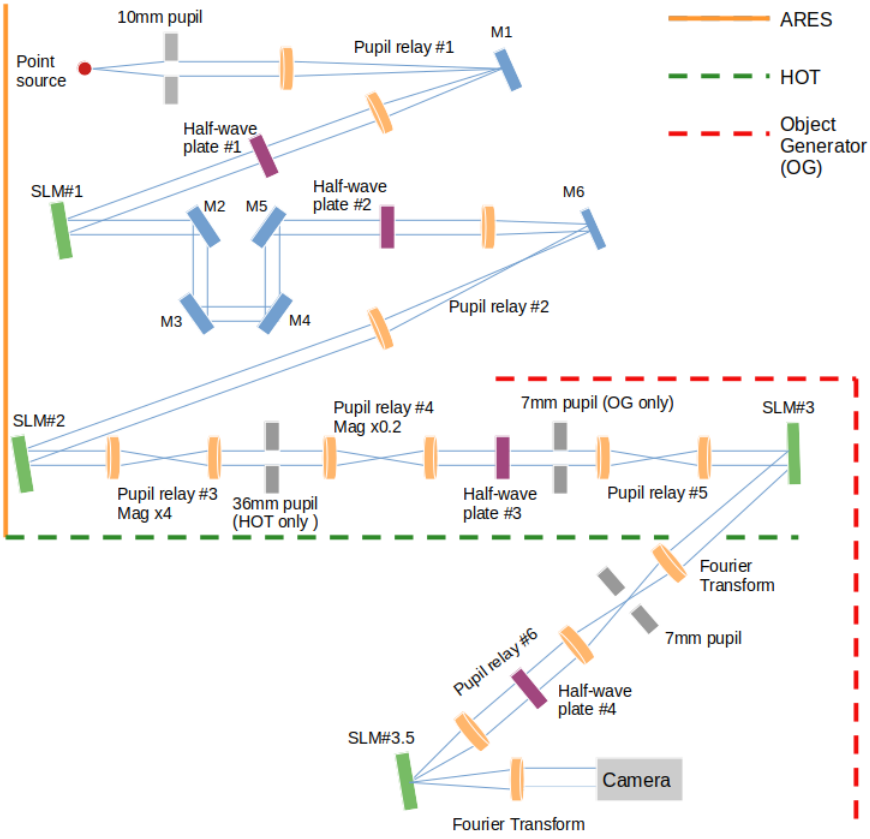

Fig. 6: ARES system with the addition of the HOT aperture and object generator concept schematic. The first section of the benchtop with the yellow outline represents the ARES system. The green dotted line signifies where the HOT system begins and ends, followed by the object generator module following the red dashed line. The HOT and the object generator experiment share an optical path, so we use different apertures for each test depending on the beam size requirements for each experiment. The 36mm pupil is only for the HOT, while the 7mm is exclusively for the object generator. Note SLM 3.5 represents the relayed path back onto SLM 3 as the second pass, separated in the schematic as SLM 3 and SLM 3.5 for simplicity.

polarization axis is optimally aligned for the SLMs' performance, minimizing the Zeroth Order Diffraction Spots (ZODS) that can't be modulated by the pixels of the SLM.

The experimental setup for the complex object generation module, shown in Figure 7, employing a dual-phase pass system, was modeled in Zemax to identify the meticulously designed system needed to ensure precise control and manipulation of wavefront properties. For the object modulation, phase one is placed on the first half of the SLM to modify the beam's wavefront. The modulated light then passes through the first lens, performing a Fourier transform on the beam, shifting it from the spatial domain to the frequency domain, creating a distribution that represents the Fourier amplitude of the desired object [10].

After the Fourier transform, the beam encounters an aperture mask placed at the focal plane. This mask maintains the modulation integrity by filtering out higher spatial frequencies beyond the desired spectrum, refining the amplitude information in the beam [20]. The beam is then relayed back onto the SLM for the second phase modulation. This modulation compensates for spurious residual phases introduced earlier in the system and refines the final phase properties to align with the target characteristics. The encoded wavefront, carrying both amplitude and phase information, passes through a final lens that performs another Fourier transform, converting the frequency components back into a spatial light distribution. The final image is then captured and analyzed using a complementary metal oxide semiconductor (CMOS) camera.

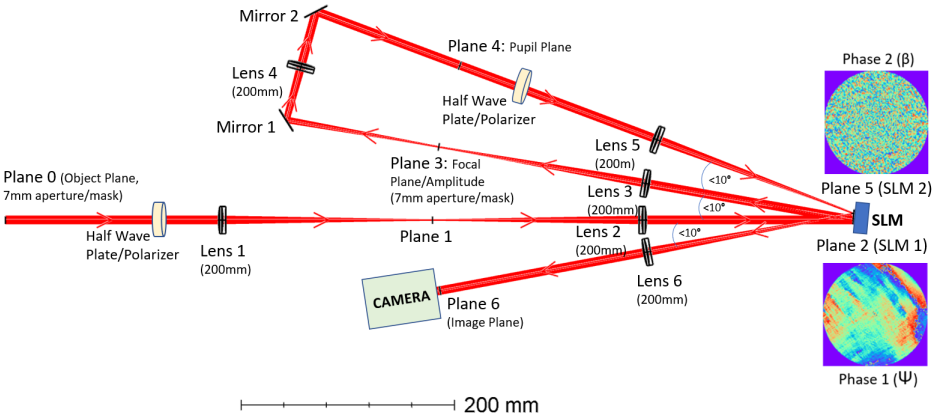

Fig. 7: Schematic of the experimental object manipulation benchtop setup. The setup uses a linearly polarized 632 nm laser, collimated by an achromatic lens (200mm), and starts with a focal plane mask creating a 7 mm aperture. A half-wave plate adjusts polarization to minimize ZODS from the SLMs. 200mm lenses relay the beam onto the SLM where the first phase is applied, followed by a 4F system for a Fourier transform utilizing three 200mm lenses. A 7mm aperture mask is placed after the first Fourier optic in the focal plane to ensure high frequency masking followed by another half wave plate for polarization adjustments. The second phase is added in the focal plane on the second half of the SLM, combining amplitude and simulated phase. A final 2F system, using one 200mm lens projects the image onto the camera sensor. SLM angles are kept below 10 degrees to ensure optimal performance.

5. RESULTS

5.1 Hybrid Optical Telescope

Using the ARES system, we observed significant changes in the PSF shape. Employing phase corrections on the SLMs, particularly SLM 3, where the phase distribution needed for the hole was applied, allowed us to create a distinguishable hole in the PSF with improved contrast in that area.

The process involved applying PD corrections through SLMs 1 and 2. Subsequently, phase screens were applied on SLM 3 to dig a hole in the PSF, as shown in Figure 8, and then superimposed with this SLM's PD correction. This figure is a collection of the predicted PSFs modeled in the simulation next to their observed shape for 3 and 40 Zernike modes. These final images represent an average of 25 photos, helping to mitigate the effects of noise and variability in the camera readings. The results show better contrast values for holes created with phase screens combining only the 3 lowest-order Zernike modes, while phase combinations using 40 Zernike polynomials maintain a distribution closer to the original HOT PSF, which is similar to what can be seen in the PSFs using the PD corrections on SLM 3. Nevertheless, the contrasts achieved two magnitudes higher than the original contrast of the intensity values in the petal where the hole is located.

After successfully generating a single-source PSF with a hole, we introduced a secondary laser to test the performance of the system with sources under different contrast conditions. The secondary laser was aligned such that its PSF peak fell within the hole of the primary laser's PSF. This process allowed for a direct comparison of contrast between using one or two sources, as seen in Figures 9 and 10, where we are using 3 and 40 Zernike polynomials for phase shaping, respectively. These PSFs look different than those of Figure 8, due to some optical misalignment that wasn't properly corrected on the day the images were captured, which explains the worse contrasts. Note how the secondary source adds noise to the image, which is expected since the intensity counts of the two PSFs are being overlapped. However, we can spot the peak of the secondary source in the location of the hole in each PSF plotted, as expected.

The method to configure the second laser involved setting the contrast by adjusting the power of the lasers to cover the dynamic range of our 8-bit camera. The primary laser's intensity was controlled to achieve a peak value of around 200 counts on the camera, while the secondary laser was adjusted to a peak value of around 20 counts, creating a contrast of approximately 10%. The value ~ 200 was chosen to ensure the camera's intensity measurements remain within the linear range with no saturation. This approach of adjusting the laser power to keep the camera readings below

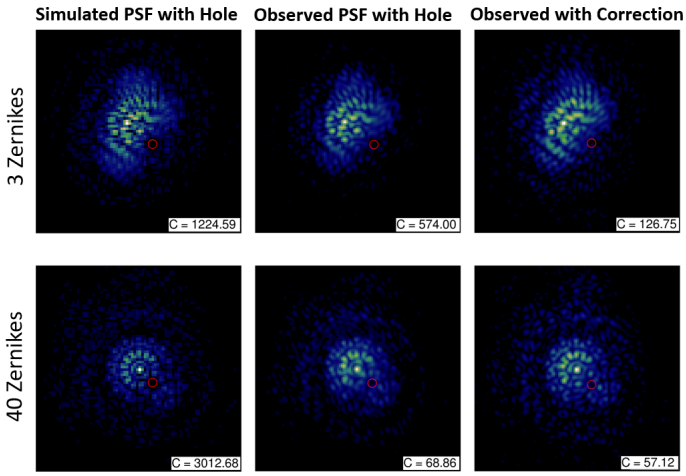

Fig. 8: Collection of all PSFs with a hole using 3 (top row) and 40 (bottom row) Zernike modes to modify the phase. The annotation in the lower right corner refers to the contrast between the total intensity inside the core (I_C) and in the hole (I_H): $C = I_C/I_H = 1/\tilde{C}$. The left plots are the predictions made by the model, indicating what we should see in the benchtop. Those pictures are the average of 25 images. The location of the hole is indicated with a red circle as a reference, but both the hole and the core are considered to be a square of 3x3 pixels, regardless of the size of the circle. The intensity values of all these PSFs were also divided by their maximum, creating a range of intensity values between 0 and 1.

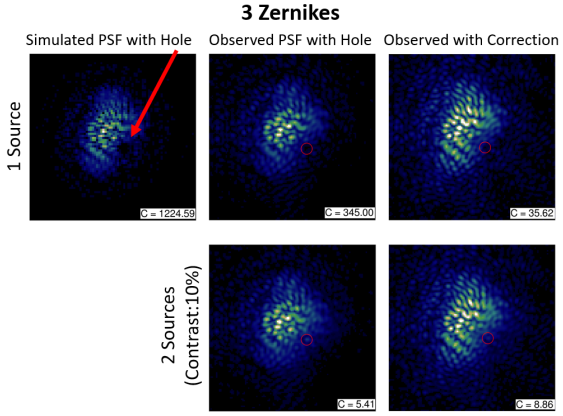

Fig. 9: Comparison between dark holes using 1 (top row) and 2 (bottom row) sources with 3 Zernike modes combined with the correction phase. The red circles and arrow indicate the hole location; larger than in single-source PSFs to make the weaker source edges more visible. Both the hole and the core are considered to be a square of 3x3 pixels. Each PSF was divided by its maximum value, so the quantities in the intensity distribution lie between 0 and 1.

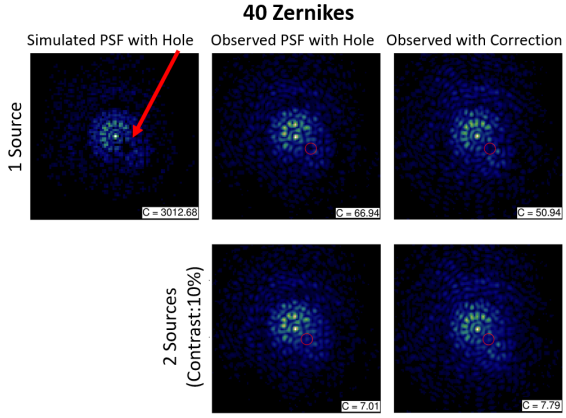

Fig. 10: Comparison between dark holes using 1 (top row) and 2 (bottom row) sources with 40 Zernike modes combined with the correction phase. The red circles and arrow indicate the hole location; larger than in single-source PSFs to make the weaker source edges more visible. Both the hole and the core are considered to be a square of 3x3 pixels. Each PSF was divided by its maximum value, so the quantities in the intensity distribution lie between 0 and 1.

approximately 200 was applied to all observed and captured images.

The observations in Figure 8 confirmed that utilizing 40 Zernike polynomials resulted in a more defined hole in the PSF compared to using only 3. Additionally, the intensity distribution more closely resembled the original HOT PSF, preserving the distinct petal-like shape that is otherwise unrecognizable with just 3 Zernike modes. These results demonstrate the effectiveness of using SLMs and phase diversity corrections within the ARES system to shape the PSF for advanced optical applications. The improvements in contrast and clarity achieved through this method indicate its potential for expanding the scope of astronomical observations and SDA.

5.2 Object Generator

Implementing the one-phase object generation module into the ARES benchtop produced similar results to the Abbott 2022 paper [1] with adjustments including applying a blazed grating to the SLM phase screen in order to mitigate the ZOD effects on the system by separating the ZODS from the reconstructed image. As shown in Figure 11, the generated HST through the dual-pass system, but utilizing only one-phase, is well removed from the zeroth order with the addition of the blaze grating and exhibits a sharp outline. However, the results exhibit unwanted speckling and reduced feature fidelity, which deviate from theoretical predictions. This reduced fidelity may be generated by a variety of practical error sources not currently modeled in the phase generation [21]. Because the dual-phase dual-pass system is extremely sensitive to alignment errors [11], the correction of this introduced error must be implemented into the dual-phase model in order to produce the accurate phases needed for manipulating the complex wavefront.

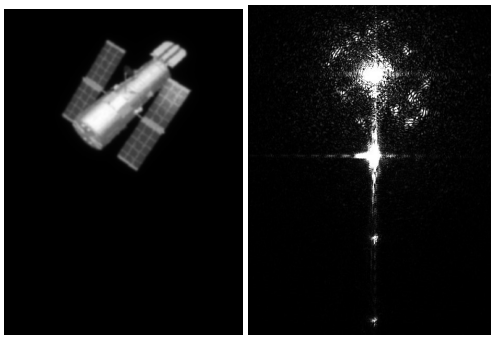

Fig. 11: Left: The original image of HST. Right: HST generated from one-phase modulation following through the entire path of the dual-pass object generator. The generated image shows effects of the ZODS impacting the center of the image and a blazed grating applied to minimize the diffracted light effects after the second SLM pass.

Fig. 12: Left: Logo from the Jesacher 2008 paper [11]. Right: Logo implemented into the dual pass object generator system with only one-phase modulation, utilizing both blazed grating and a polarizer showing minimization of the ZODS effects.

To further show the affects from the dual-pass system, Figure 12 shows the logo image used from the Jesacher 2008 paper [11] utilizing only one-phase modulation, but propagating through the dual pass system. The one-phase technique through the two Fourier optics or dual-pass system was used to reduce the ZODS, confirm optimal alignment and show the benchtop propagation effects, not currently implemented in the phase optimization model. Similar to the one-phase HST image in Figure 11 the outline of the image is the most prominent. However, despite improved alignment and reducing ZODS affects, the second pass system remained ineffective in constructing a higher fidelity image, proving further details needed in the modeling of the two phases before implementing into the system.

5.3 Complex Object Generator System Constraints and Sources of Error

The analysis of the system constraints focused on the spectral frequency limits of the dual-phase approach. Given the maximum resolvable spectral frequency of $\frac{1}{\lambda \cdot \text{focal length}}$ and the smallest resolvable frequency of $\frac{D}{\lambda \cdot \text{focal length}}$, the system appears to be operating near the resolution limits of its optical components. The pixel size of the SLM corresponds to a physical discretization of spatial frequencies, imposing specific bounds on the system's performance. In real space, the phase pattern generated by the SLM is constrained by the pixel size, which filters the "true" object such that the smallest resolvable feature size is 8 μm. Consequently, the Fourier modulus on the other side of the lens cannot be formed smaller than this resolvable feature size. The constraint due to the SLM pixel size is not the cutoff frequency

of the system but rather a filtering effect due to discretization. The Nyquist criterion confirms that the smallest feature size supported in object space is two times the pixel size. Therefore, object features must be larger than $2\delta_{\text{SLM}}$, where δ_{SLM} is the SLM pixel size, and the object height must be smaller than $\frac{\text{focal length}\lambda}{\delta_{\text{SLM}}}$ to avoid image degradation.

The success of the dual-pass object generator is predicated on the assumption that it operates as a diffraction-limited system. However, real-world imperfections present significant challenges to this assumption. A Zemax model was used to evaluate the cumulative effects of residual design aberrations, revealing that the resulting geometric PSF is comparable in size to the Airy disk diameter. This finding indicates that the nominal design is at the threshold of being a diffraction-limited system, leaving little to no margin for manufacturing errors, assembly errors, and alignment errors associated with the realized benchtop system.

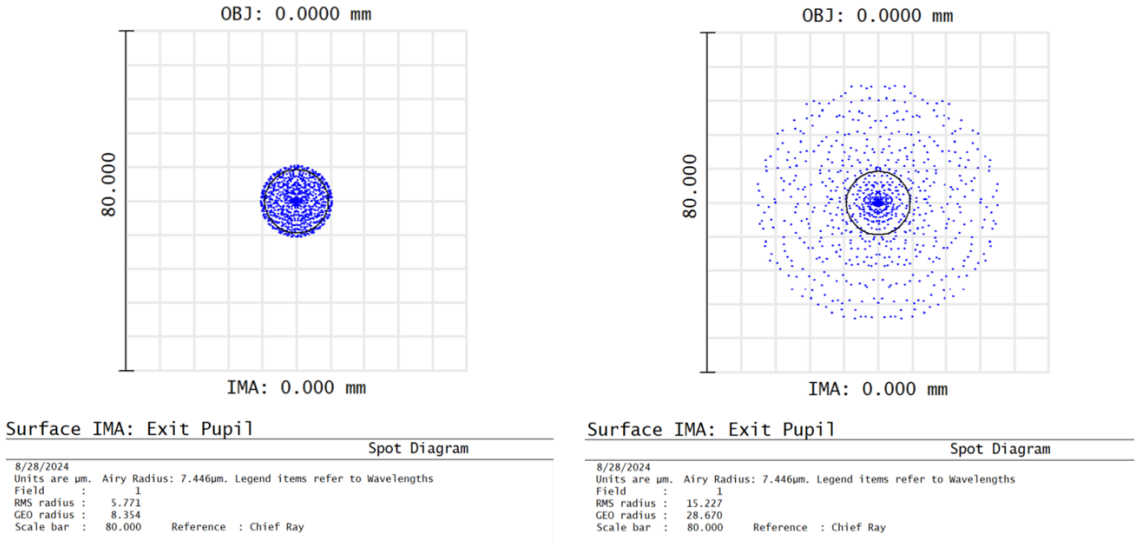

Fig. 13: The Zemax model on the left indicates a diffraction-limited perfect system, represented by the alignment or ideal placement of the spot size and Airy disk (black and blue circles). The right Zemax model shows the effects of the system with an alignment or placement error of only 0.5 mm, demonstrating that it is no longer diffraction-limited.

The Zemax simulations further demonstrated that tilt and decenter errors of as little as 1 mm—equivalent to 2 percent of the lens diameter—and tilts of 2 degrees produced geometric errors of a similar magnitude. Moreover, vendor tolerances in focal lengths, along with cumulative placement errors, can introduce magnification inaccuracies, leading to misalignments and optical system degradation. To maintain diffraction-limited performance, precise alignment and calibration are essential. The system's performance is further affected by potential errors such as nonlinearities, phase and intensity aberrations, plane misalignments, and SLM edge effects, all of which challenge the assumption of a diffraction-limited system.

The discrepancies between the idealized simulation model and the actual benchtop setup reveal the need for model adjustments to better reflect real-world conditions. The current model overlooks challenges like alignment stability and beam quality [22], which are crucial for accurate hologram reconstruction. Additionally, using the edges of the SLM instead of the center introduces further phase and amplitude errors, reducing aperture effectiveness and increasing sensitivity to misalignments and non-linearities.

5.4 Proposed Solutions and Optimization

To address these challenges, several strategies are proposed. These include incorporating wavefront sensing, simplifying the optical layout, utilizing two SLMs with center phase construction, and overfilling the lens aperture to reduce focus ambiguity. Mechanical alignment to achieve the necessary precision, can be improved with the use of additional equipment, such as point source microscopes to locate focal planes, precision rails, and opto-mechanical fixtures to index the optical surface of the SLM to its mechanical surface across multiple reference datums. Additionally, optimizing the phase masks for the system's specific parameters—including wavelength, focal length, and Fourier domain scaling—could enhance the performance of the dual-phase system.

6. CONCLUSION

This research presents advancements in the development of optical simulation technologies, specifically through the integration of the Hybrid Optical Telescope (HOT) system with an object generation module within the Advanced Reconnaissance of Earth-orbiting Satellites (ARES) platform. By leveraging adaptive optics and precise phase manipulation techniques, we have successfully demonstrated the ability to engineer point spread functions (PSFs) with tailored characteristics, such as creating dark holes for enhanced observation of faint objects near brighter sources. The study of the dual-phase modulation technique identified key steps needed for its implementation into the system, while the successful application of the one-phase method underscores the system's versatility and potential for high-fidelity optical simulations. It also offers a path toward more complex and precise wavefront manipulation, essential for advancing both astronomical observations and space situational awareness.

Future work will involve refining the phase correction techniques to further improve the contrast and resolution of the PSF. We will explore the integration of amplitude corrections alongside phase modifications to strengthen the fidelity of the PSF and reduce unwanted artifacts in the final image. Additional tests will be conducted using multiple light sources and more complex phase modifications, including the simulation of atmospheric turbulence and light propagation effects, to fully evaluate the capabilities of the enhanced ARES system. The focus will remain on refining the dual-phase modulation techniques employed in the system to overcome current limitations, thereby improving our ability to simulate optical phenomena with greater accuracy. Optimization techniques include incorporating wavefront sensing, simplifying the optical layout, utilizing two SLMs with center phase construction, overfilling the lens aperture and mechanical alignment improvements using a point source microscope, alignment fixtures, optical rails, and precision focusing spheres. Future developments of the benchtop will expand the range of conditions and objects that can be accurately represented, opening new vistas for both optical research and applications, deepening our understanding of optical science, particularly in observational astronomy and space surveillance.

This study lays the groundwork for future advancements in optical physics, with broad implications for both scientific research and industrial applications. By continuing to refine and optimize the ARES system, particularly through the development of more robust dual-phase modulation techniques, future research can achieve even greater accuracy in simulating and analyzing complex optical phenomena. The scalability and adaptability of this benchtop system makes it a valuable tool for ongoing and future explorations in optical science, enhancing our understanding of both terrestrial and extraterrestrial environments.

ACKNOWLEDGMENTS

I would like to express my gratitude to my colleagues at the Georgia Tech Research Institute (GTRI) for their expertise and assistance in navigating the complexities of this project, including Nathan Meraz, Joseph Greene, Katie Twitchell, and Douglas Hope. I am also grateful to Dan Johns and Stuart Jefferies at Georgia State University for providing support in the lab as well as modeling and simulation guidance during various stages of this work.

REFERENCES

[1] Caleb Abbott et al. Ares: a versatile benchtop testbed for evaluating techniques for imaging through atmospheric turbulence. In *2022 Advanced Maui Optical and Space Surveillance Technologies Conference*, 2022.

[2] François Roddier. *Adaptive optics in astronomy*. Cambridge University Press, 1999.

[3] Joss Bland-Hawthorn and Pierre Kern. Astrophotonics: a new era for astronomical instruments. *Optics Express*, 17(3):1880, January 2009.

[4] Tom D. Milster, P. P. Banerjee, and V. Fadeyev. Adaptive optics with diffractive optical elements: design and analysis. *JOSA A*, 36(12):D31–D44, 2019.

[5] Svetlana V Berdyugina, Jeff R Kuhn, Maud Langlois, Gil Moretto, Joshua Krissansen-Totton, D Catling, JL Grenfell, Tina Santl-Temkiv, Kai Finster, J Tarter, et al. The exo-life finder (elf) telescope: New strategies for direct detection of exoplanet biosignatures and technosignatures. In *Ground-based and Airborne Telescopes VII*, volume 10700, pages 1453–1466. SPIE, 2018.

[6] Olivier Guyon. Phase-induced amplitude apodization of telescope pupils for extrasolar terrestrial planet imaging. *Astronomy & Astrophysics*, 404(1):379–387, 2003.

[7] John T. Trauger and Wesley A. Traub. A laboratory demonstration of the capability to image an earth-like extrasolar planet. *Nature*, 446(7137):771–773, 2007.
[8] N. Jeremy Kasdin, Robert J. Vanderbei, David N. Spergel, and Mark G. Littman. Extrasolar planet finding via optimal apodized-pupil and shaped-pupil coronagraphs. *The Astrophysical Journal*, 582(2):1147–1161, 2003.
[9] D. Hope. High-resolution imaging of closely spaced objects with high contrast ratios. In *Advanced Maui Optical and Space Surveillance Technologies Conference*, 2019.
[10] Robert K Tyson. *Principles and applications of Fourier optics*. IOP Publishing, Bristol, UK, 2014.
[11] Alexander Jesacher et al. Near-perfect hologram reconstruction with a spatial light modulator. *Optics Express*, 16(4):2597–2603, 2008.
[12] Justo Arines and Ana García. Wavefront-based spatial light modulator alignment. *Optical Engineering*, 59(4):041206–041206, 2020.
[13] Liesl Burger, Igor A Litvin, and Andrew Forbes. Simulating atmospheric turbulence using a phase-only spatial light modulator. *South African Journal of Science*, 104(3):129–134, 2008.
[14] Arun K. Majumdar. *Laser-Based Satellite and Inter-satellite Communication Systems: Advanced Technologies and Performance Analysis*, pages 199–229. Springer International Publishing, Cham, 2022.
[15] John P. Dakin and Robert G. W. Brown. *Handbook of Optoelectronics (Second Edition): Concepts, Devices, and Techniques*. CRC Press, 2010.
[16] Mei-Li Hsieh, Mao-Ling Chen, and Chau-Jern Cheng. Improvement of the complex modulated characteristic of cascaded liquid crystal spatial light modulators by using a novel amplitude compensated technique. *Optical Engineering*, 46(7):070501, 2007.
[17] E O'Neill. Spatial filtering in optics. *IRE Transactions on Information Theory*, 2(2):56–65, 1956.
[18] Noriaki Miura. Blind deconvolution under band limitation. *Optics Letters*, 28(23):2312–2314, 2003.
[19] Stuart Jeffries. Personal communication, 2024. Verbal discussion.
[20] David Blinder, Tobias Birnbaum, Tomoyoshi Ito, and Tomoyoshi Shimobaba. The state-of-the-art in computer generated holography for 3d display. *Light: Advanced Manufacturing*, 3(3):572–600, 2022.
[21] Rochester Institute of Technology. Simulated phase noise for adaptive optics, 2019. Accessed: 2024-07-28.
[22] Department of Defense. Diffractive optical elements for laser beam shaping. Technical report, Defense Technical Information Center, 1991.